RESEARCH ARTICLE
SPACE PHYSICS

Earth and Planetary Physics
8: 632–640, 2024
doi: 10.26464/epp2024029

Inversion of $O_2$1.27 μm nightglow emissions: A climatological analysis using satellite Limb-Viewed spectra and Harmonic analysis method

YiYi Sui[1,2,3], YaJun Zhu[1,2,3,4*], QiuYu Chen[1,3], MaoSheng He[1,3,4], and JiYao Xu[1,2,3,4]

[1]State Key Laboratory of Space Weather, National Space Science Center, Chinese Academy of Sciences, Beijing 100190, China;

[2]University of Chinese Academy of Sciences, Beijing 100190, China;

[3]Key Laboratory of Solar Activity and Space Weather, National Space Science Center, Chinese Academy of Sciences, Beijing 100190, China;

[4]Hainan National Field Science Observation and Research Observatory for Space Weather, National Space Science Center, Chinese Academy of Sciences, Beijing 100190, China

Key Points:

- Volume Emission Rates (VERs) of O_2 1.27 μm nightglow were retrieved from satellite limb-viewed spectra by application of a linear global algorithm.
- The retrieved volume emission rates show good consistency with the Sounding the Atmosphere by Broadband Emission of Radiation (SABER) observations; they exhibit annual maxima at approximately 90 km above the equator.
- Temporal variations (annual and semi-annual) of volume emission rates were revealed, showing solar cycle dependence.

Citation: Sui, Y. Y., Zhu, Y. J., Chen, Q. Y., He, M. S., and Xu, J. Y. (2024). Inversion of $O_2$1.27 μm nightglow emissions: A climatological analysis using satellite Limb-Viewed spectra and Harmonic analysis method. *Earth Planet. Phys.*, *8*(4), 632–640. http://doi.org/10.26464/epp2024029

Abstract: This study employs a linear inversion algorithm to retrieve volume emission rates (VERs) of molecular O_2 nightglow at 1.27 μm, utilizing Limb-Viewed spectra obtained from the SCanning Imaging Absorption spectroMeter for Atmospheric for CHartographY (SCIAMACHY) payload on board the Envisat satellite. The retrieved results are compared with VERs data from the SABER payload on the Thermosphere Ionosphere Mesosphere Energetics and Dynamics (TIMED) satellite, exhibiting consistency. This will help to facilitate accurate revelation of spatial distribution and periodic variation in O_2 nightglow. VERs are extracted monthly within the altitude range of 75–110 km from 2002 to 2012, yielding a climatology of spatial and temporal distributions. The meridional structure exhibits two maxima, at the equator and at 45°N. Between August and October, the VERs exhibit a meridional bimodal structure, with the weaker one above the equator and the stronger one above 45°N. In April, the VERs reach their annual maximum. Additionally, harmonic analysis reveals significant temporal variations on different scales. The emission shows characteristics of annual and semi-annual variation, and a non-linear long-term trend associated with solar cycle activity.

Keywords: VERs; $O_2$1.27 μm nightglow; SCIAMACHY

1. Introduction

As an important tracer for the atmospheric photochemical and dynamical processes in the middle and upper atmosphere, the airglow is widely used to study the mechanisms of these processes due to the joint influence of atmospheric oscillations and external solar radiation (Xu JY et al., 2012; Yang XJ et al., 2020; Wang WJ et al., 2021). Oxygen molecules have seven electronic energy levels, which means the transition between different energy levels can produce airglow in different bands. Among these bands, the 1.27 μm airglow is the product of spontaneous radiation of excited oxygen molecules returning to the fundamental state ($O_2(a^1\Delta_g \rightarrow X^3\Sigma_g)$). The 1.27 μm airglow is one of the commonly used sources to investigate the physical characteristics of the middle and upper atmosphere.

In the 1970s and 1980s, rocket-based measurements were the main detection method of $O_2$1.27 μm nightglow. For example, the Energy Transfer in the Oxygen Nightglow (ETON) program explored the emission profile of $O_2$1.27 μm nightglow to analyze the photochemical and radiative mechanisms in the nightglow formation processes (McDade et al., 1987; Lopez-Moreno et al., 1988). The S-310-16 rocket project, combined with a ground-based grating monochrometer, initially clarified the transmission process of the $O_2$1.27 μm nightglow from the generation layer to the ground (Yamamoto et al., 1992). However, early rocket

First author: Y. Y. Sui, suiyiyi21@mails.ucas.ac.cn
Correspondence to: Y. J. Zhu, y.zhu@swl.ac.cn
Received 18 APR 2024; Accepted 20 JAN 2024.
First Published online 21 JUN 2024.

measurements had some limitations. For example, the instantaneity and discontinuity of the observations made them unsuitable for any global, long-duration, understanding of the distribution characteristics of nightglow emission. Satellite remote sensing technology can overcome these limitations; spaceborne instruments can provide data demonstrating the airglow's vertical variation by limb-scan observation, greatly aiding study of the three-dimensional spatial structure and temporal variations of the middle and upper atmosphere (Wang YP et al., 2016; Li HC, 2023). The Solar Mesosphere Explorer (SME) satellite launched in 1984 was able to measure the oxygen airglow continuously for more than 12 hours per day. Based on the long-term observations of the SME mission, Howell et al. (1990) deduced the corresponding photochemical reaction mechanism. Gao H et al. (2011) revealed the global distribution characteristics of OH airglow and O_2 1.27 μm nightglow from 2002 to 2010 based on airglow data detected by the SABER payload. Zarboo et al. (2018) retrieved the dayglow and nightglow VERs of the $O_2(b^1\Sigma_g^+)$ band and $O_2(a^1\Delta_g)$ band from airglow limb observations made at an altitude of 70–150 km by the SCIAMACHY payload, using the least square method. Li AQ et al. (2020) retrieved the $O_2$1.27 μm dayglow VERs based on observations from the Optical Spectrograph and Infrared Imaging System (OSIRIS), and discussed correlation of VERs with the number density of daytime ozone.

Research on the $O_2$1.27 μm airglow has gradually expanded to other fields. The wavelength band of this airglow is close to the the CO_2 absorption band; thus the uncertainty was small when it was used as an index of the atmospheric path length. The atmosphere's greenhouse gas content can also be monitored by the radiative intensity of $O_2$1.27 μm airglow (Sun K et al., 2018; Bertaux et al., 2020). Since the $O_2$1.27 μm airglow has relatively strong emission and weak self-absorption in the Mesosphere and Lower Thermosphere (MLT) region, it is an ideal precursor for detecting atmospheric wind and temperature fields (He WW et al., 2019). For example, Sun K et al. (2022) used Bayesian inversion to retrieve temperature profiles by minimizing the difference between simulated and observed limb radiance spectra, using a priori regularization.

As mentioned above, systematic research on the long-term variation and spatial distribution of $O_2$1.27 μm nightglow has been relatively lacking. The $O_2$1.27 μm nightglow dataset from the SCIAMACHY payload has the advantages of long continuous observation time and high resolution at night, allowing detailed analysis of the periodic variation and spatiotemporal characteristics of nightglow. In this study, based on monthly average spectra from the SCIAMACHY payload, VERs of $O_2$1.27 μm nightglow from 2002 to 2012 are retrieved using a linear global optimization algorithm, and the accuracy of the inversion algorithm is evaluated. Furthermore, the spatial structure and temporal variation of the VERs of $O_2$1.27 μm nightglow in the MLT region are analyzed, and the periodic variation of oscillation frequency is summarized through harmonic analysis.

This paper is organized as follows: Section 2 introduces the instruments, datasets, and analysis methods. Section 3 describes the $O_2$1.27 μm nightglow VERs results obtained from linear inversion, including characteristics of the nightglow's spatiotemporal distribution and periodic variation, and briefly discusses a possible physical mechanism. Section 4 summarizes our findings.

2. Data and Methods

2.1 Data

As a passive detection instrument, SCIAMACHY is part of the atmospheric chemistry payload on the Envisat satellite launched by the European Space Agency (Bovensmann et al., 1999). Envisat was in service from March 2002 to April 2012 and operated on a polar sun-synchronous orbit, with 14 tracks per day and 35 days global coverage. The instrument covered the tangent altitude range of 75–150 km through limb observation, with a vertical spacing of 3.3 km (Sun K et al., 2022). It is worth mentioning that nighttime limb measurements were all taken at 22:00 Local Solar Time (LST) (von Savigny, 2015). SCIAMACHY was tasked with observing all atmospheric radiation in the wavelength range of 280–2380 nm (Bovensmann et al., 1999). Figure 1 illustrates the geographical coverage of SCIAMACHY nighttime limb measurements as a function of time and latitude. As a whole, the maximum latitude at which data could be collected in the northern hemisphere was 77.5°N; in the southern hemisphere, the maximum latitude was 47.5°S. In this study, Level 1 data in channel 6 (1200–1360 nm) are used, which are monthly zonal mean $O_2$1.27 μm nightglow spectra, in 5° latitude bins.

2.2 Retrieval Method

First, spectral data from SCIAMACHY are preprocessed. Two defective pixels at 1262 nm and 1282 nm in the $O_2(a^1\Delta_g)$ band are excluded, and the average spectral intensity above 110 km is then considered as a background value, as follows: According to previous studies, the main altitude range of the $O_2$1.27 μm nightglow distribution is 80–110 km (McDade et al., 1987; Lopez-Moreno et al., 1988). Information collected by the instrument above 110 km is thus mainly from radiation in the background atmosphere rather than the nightglow emissions, so the data beyond this altitude is regarded as background values. To eliminate the atmospheric background effect, this average value is subtracted from all valid data.

Figure 2 displays the distribution of spectral intensity at different heights after background value filtering. The wavelength sampling interval in Figure 2 is approximately 0.76 nm. The spectral

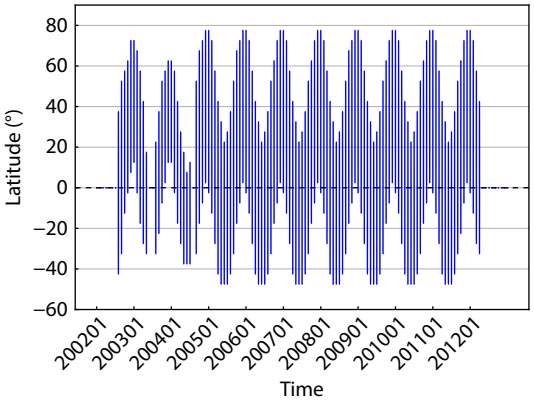

Figure 1. Latitude coverage of SCIAMACHY limb nighttime observations.

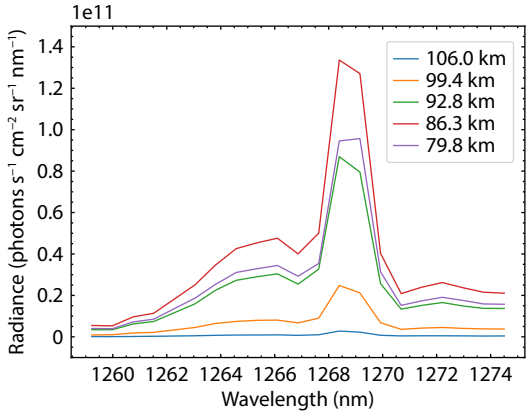

Figure 2. Nightglow spectral intensity around $O_2$1.27 μm at various altitudes, observed at 30–35°N in April 2008.

data, processed through the aforementioned steps, are now ready for subsequent linear global optimization inversion.

In this study, the maximum posterior (MAP) method is used to do a linear global optimization inversion to obtain the VERs (Rodgers, 2000). The fundamental equations of the algorithm are outlined below:

$$\hat{\boldsymbol{x}} = \boldsymbol{x}_a + \boldsymbol{G}\left(\boldsymbol{y} - \boldsymbol{K}\boldsymbol{x}_a\right), \tag{1}$$

$$\boldsymbol{G} = \left(\boldsymbol{K}^{\mathrm{T}}\boldsymbol{S}_e^{-1}\boldsymbol{K} + \boldsymbol{S}_a^{-1}\right)^{-1}\boldsymbol{K}^{\mathrm{T}}\boldsymbol{S}_e^{-1}, \tag{2}$$

where $\boldsymbol{x}_a$ is the mean value of the prior information, $\boldsymbol{S}_a$ is the covariance of the prior information, $\boldsymbol{y}$ is the spectral radiance measured by SCIAMACHY, $\boldsymbol{S}_e$ is the error covariance matrix of the spectral radiance, and $\boldsymbol{K}$ is expressed as the weight function representing the linear relationship between the VER and the spectral radiance. The inverted VER is denoted as $\hat{\boldsymbol{x}}$.

Note that in the maximum posterior method, the $\boldsymbol{x}_a$ is a zero matrix, which means the prior information is set to zero. $\boldsymbol{S}_a$ is a matrix with a constant value of 1.1×10^{-5} photons s^{-1} cm^{-3} for diagonal elements, representing altitudes between 70 km and 110 km which then exponentially decays to zero for grid points above and below these levels (Li AQ et al., 2021). Considering that the self-absorption effect of oxygen becomes more significant below 60 km (Sun K et al., 2022), and that the target altitude of this study is above 70 km, we ignore the influence of O_2 self-absorption. The loss in the radiative transmission path is not taken into account, meaning that the matrix $\boldsymbol{K}$ denotes essentially the optical path length of each layer scanned by the spaceborne instrument.

In addition, the quality of the inversion is evaluated by the average kernel Matrix (AVK Matrix), abbreviated as $\boldsymbol{A}$, calculated with the following equation:

$$\boldsymbol{A} \equiv \frac{\partial \hat{\boldsymbol{x}}}{\partial \boldsymbol{x}} = \boldsymbol{G}\boldsymbol{K}. \tag{3}$$

This matrix represents the extent of deviation from the actual state with respect to vertical resolution. As shown in Figure 3a, within the range of 80–100 km, the measurement contribution (sum over each row of the averaging kernel) is approximately one, and the averaging kernels peak at the corresponding tangent altitudes. Figure 3b illustrates that the vertical resolution is 3.3 km, which closely aligns with the sampling distance measured by SCIAMACHY.

3. Results and Discussion

3.1 Inversion Results

An independent emission profile can be derived by integrating the inverted VER of each individual spectral line along the entire band. An example is illustrated in Figure 4, displaying the altitudinal variation of the $O_2^1\Delta$ band nightglow VERs in the wavelength range of 1260–1271 nm. The peak of the nightglow band-VER is 9.5×10^4 photons s^{-1} cm^{-3}, occurring at an altitude of approximately 90 km.

The linear inversion results of SCIAMACHY and monthly zonal mean SABER VERs are shown in Figures 5a and b. Compared with Figures 5a and b, the spatial structure of the inversion results resembles the data detected by SABER, showing similar peak height and peak value above the equatorial region. The VER peak of nightglow emission is $20–25 \times 10^4$ photons s^{-1} cm^{-3} and the peak height is 86–88 km. However, as shown in Figure 5c, there is bias between the two datasets, with the calculated average deviation being approximately -1.3×10^4 photons s^{-1} cm^{-3}. The largest

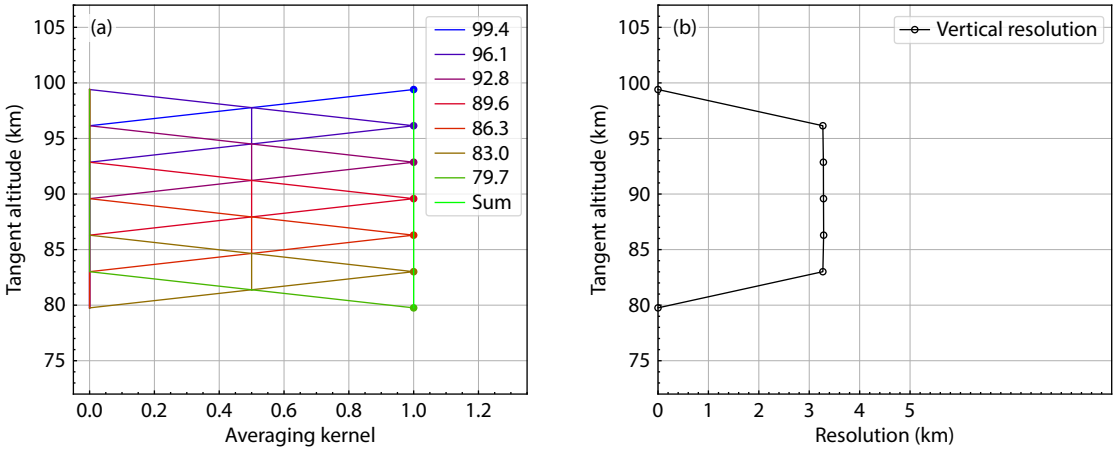

Figure 3. The averaging kernel and the vertical resolution of the retrieval at 0–5°N in April 2008.

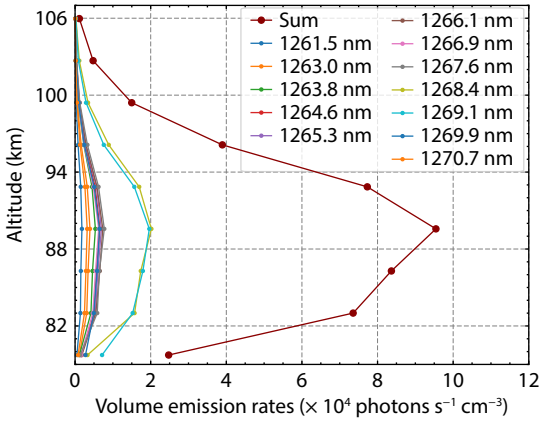

Figure 4. The inverted VERs of nightglow emissions in different wavelengths at 20–25°N in April 2010. The dark red line represents the integrated VERs of each individual limb spectrum.

deviation, approximately 40%, appears at 90 km. The large bias between the two datasets, possibly due to the different detection principles of the two instruments. It is worth mentioning again that the two datasets are *monthly zonal mean* data. Figure 6 shows the profiles of oxygen nightglow VERs from the two different datasets as a function of latitude and altitude. The SCIAMACHY dataset at 40°S–10°N is systematically smaller than the SABER dataset, with a maximum deviation of 25%; at 10–40°N, however, the two datasets demonstrate relatively consistent results.

3.2 Spatial and Temporal Distribution

Figure 7 shows the contours of $O_2$1.27 μm nightglow VERs in 2007, as inverted using the linear algorithm as a function of latitude and altitude. Due to changes in the satellite's orbit, the latitude coverage measured by SCIAMACHY was limited. In the mesopause region above the equator, the $O_2$1.27 μm nightglow emission reveals evident annual and semi-annual variations, with similar annual variations appearing at mid-latitudes in the northern hemisphere. The data from March reveal two distinct emission peaks in the mesopause region, with one peak at 88 km above the equator and a weaker one at 91 km above the latitude of 60°N. The maximum annual VER was recorded in April with a value of around 2 × 10^5 photons s^{-1} cm^{-3}; the peak altitude was around 88 km. In September, two peaks appeared, with the weaker one at 88 km above the equator and the stronger one at 90 km above the latitude of 45°N. In March, by contrast, the stronger peak was above the equator. The bimodal structure in October closely mirrors that observed in September. In November and December, the intensity of VERs over the 45°N region decreased significantly, and the gap with the equator region gradually widened.

Figure 8 illustrates the time-altitude distribution of $O_2$1.27 μm nightglow VERs inverted by the linear algorithm from 2002 to 2012. The altitude range is 79–96 km, and the inverted VERs outside this interval are very small, at least an order of magnitude smaller than the peak. Comparing the intensity of the $O_2$1.27 μm nightglow VERs from 2002 to 2012, it appears that the VERs show a relatively strong dependence on solar activity, although the dataset does not cover a complete 11-year cycle. In 2002–2003, with maximum solar activity, $O_2$1.27 μm nightglow reached a corresponding peak in emission. Subsequently, as solar activity decreased and reached its minimum at the end of 2008 and beginning of 2009, the intensity of $O_2$1.27 μm nightglow experienced a trough. With the beginning of a new solar cycle, the increasing solar activities led to a gradual increase in the VERs of $O_2$1.27 μm nightglow. As shown in Figure 8, the intensity of nightglow regained its peak in April 2012. Figure 8 also shows that the responses to solar radiation vary with latitude. The average emission intensity near the equator region is significantly stronger than that at 20°N, which is generally consistent with the results of Gao H et al. (2016); they analyzed the 13-year average oxygen nightglow intensity to study the response to solar radiation and pointed out a large peak around the equator, two small peaks around 35°S/N, and two valleys around 20°S/N.

As shown in Figure 8, over the past 11 years the intensity of the oxygen nightglow VERs was stronger in spring and summer than in autumn and winter. Two peaks and one valley occur each year — the valley in July, the first peak in April, and the second peak in October, albeit with lower intensity than the April peak. This pattern is consistent with the conclusions of Gao H et al. (2016),

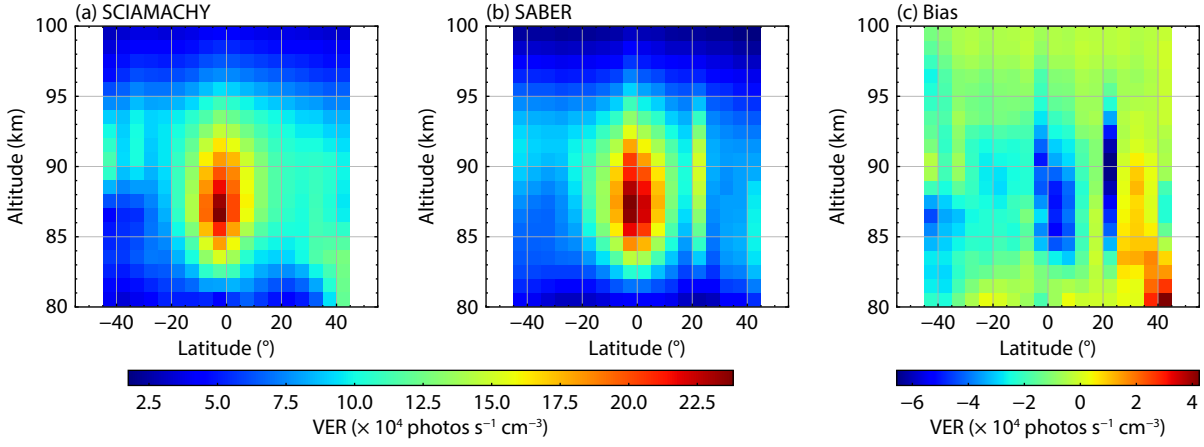

Figure 5. (a) Distribution of inverted VERs based on SCIAMACHY observations in April 2007. (b) Distribution of VERs in April 2007 after filtering from SABER measurements. (c) Distribution of difference between the inverted VERs and filtered data from SABER. The black and orange error bars represent the uncertainty of the inversion results and of the SABER filtered dataset, respectively.

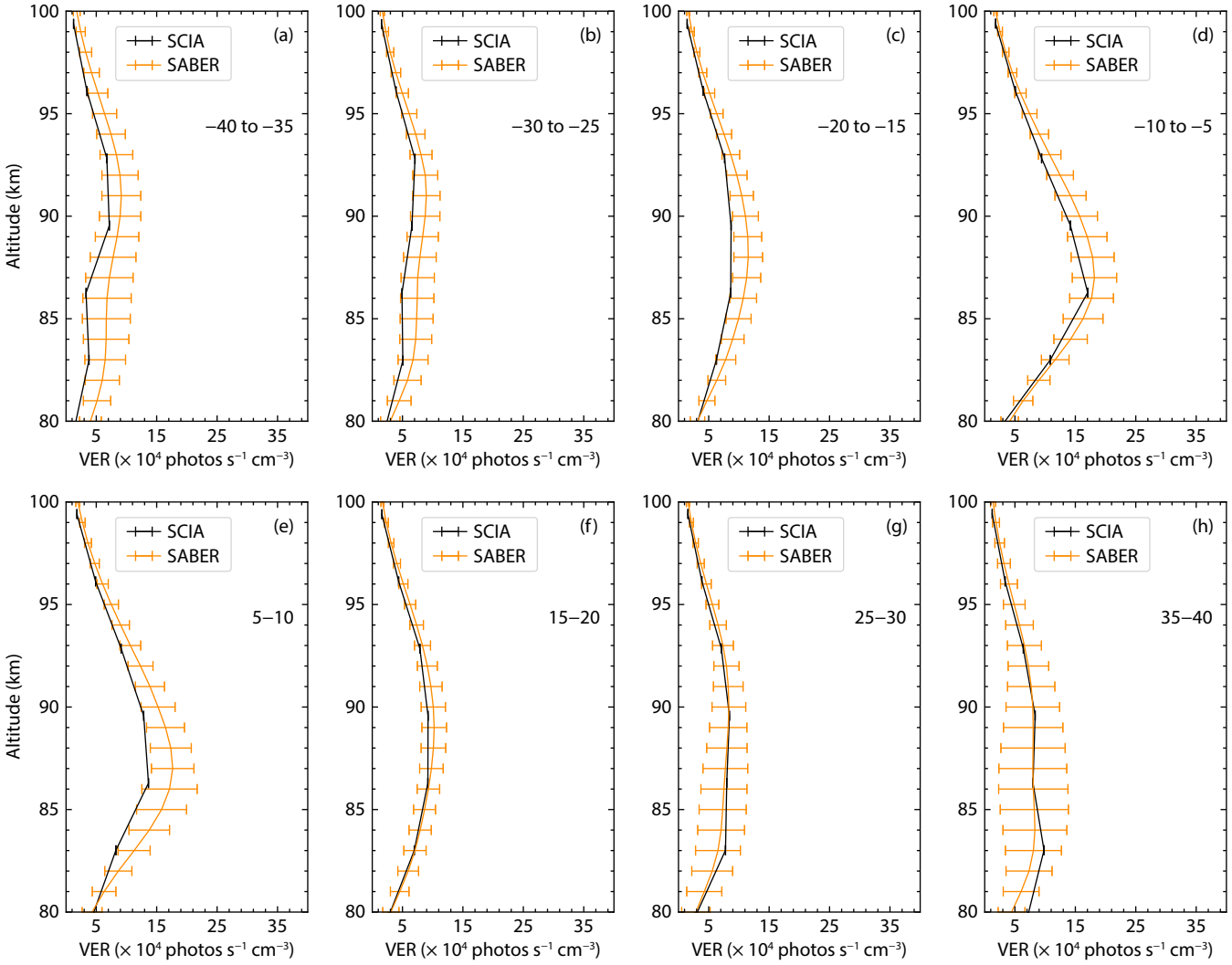

Figure 6. Comparison of VERs between two datasets at different latitudes and altitudes. The orange lines represent the SABER filtered dataset; the black lines represent the inversion results from the SCIAMACHY dataset. Panels (a)–(d) give results for the southern latitude region; panels (e)–(h) present results for the northern latitude region.

that seasonal variations dominate the time series of oxygen nightglow intensity at all latitudes.

3.3 Oscillation Period

To quantitatively analyze the temporal variation of inverted $O_2$1.27 μm nightglow VERs, we used harmonic analysis to extract semi-annual, annual and 11-year solar cycle variations. All the VERs of each latitude point in the altitude range of 79–106 km per month were added and summed to obtain a dataset suitable for harmonic analysis. The polynomial fitting algorithm was then applied to determine the short-term variation and long-term tendency of the oscillation frequency. The multiple linear regression analysis used the following equation:

$$y = A_{\mathrm{SAO}}\cos\left[\frac{2\pi}{6}(t-P_{\mathrm{SAO}})\right] + A_{\mathrm{AO}}\cos\left[\frac{2\pi}{12}(t-P_{\mathrm{AO}})\right] + A_{\mathrm{QBO}}\cos\left[\frac{2\pi}{24}(t-P_{\mathrm{QBO}})\right] + A_{F10.7}F_{10.7}(t\text{-shift}) + \mathrm{offset}, \quad (4)$$

where, $F_{10.7}$ is the $F_{10.7}$ cm solar flux proxy in units of 10^{-22} Wm^{-2} Hz^{-1} (Tapping, 2013), and t represents months. $A_{F10.7}$ is the amplitude of the $F_{10.7}$ cm solar flux. A_{SAO}, A_{AO}, P_{SAO} and P_{AO} are the amplitudes and phases of the Semi-Annual Oscillation (SAO) and Annual Oscillation (AO), respectively. A_{QBO} and P_{QBO} are the amplitudes and phases, respectively, of the Quasi-Biennial Oscillation (QBO) corresponding to 24 months. The fitting parameters include the amplitudes and phases of the SAO, AO and QBO, supplemented by a factor ($A_{F10.7}$) scaling the $F_{10.7}$ cm solar flux proxy, and a constant term. The "shift" is the time lag of the solar cycle impact while the "offset" is the mean value of the time series (Zhu YJ, 2016).

Figure 9 displays the harmonic analysis results of inverted $O_2$1.27 μm nightglow VERs at 10–15°N. The SAO maximizes in April and October, and minimizes in June and January. It shows an amplitude of about 9.4%. In addition, the AO has a maximum near the summer and a minimum near the winter and its amplitude is about 9.0%. Annual mean differences of VERs between the maximum (2002) and minimum (2008) of the 23rd solar cycle reveal variations of 19.8%.

The semi-annual and annual variations in the inverted $O_2$1.27 μm

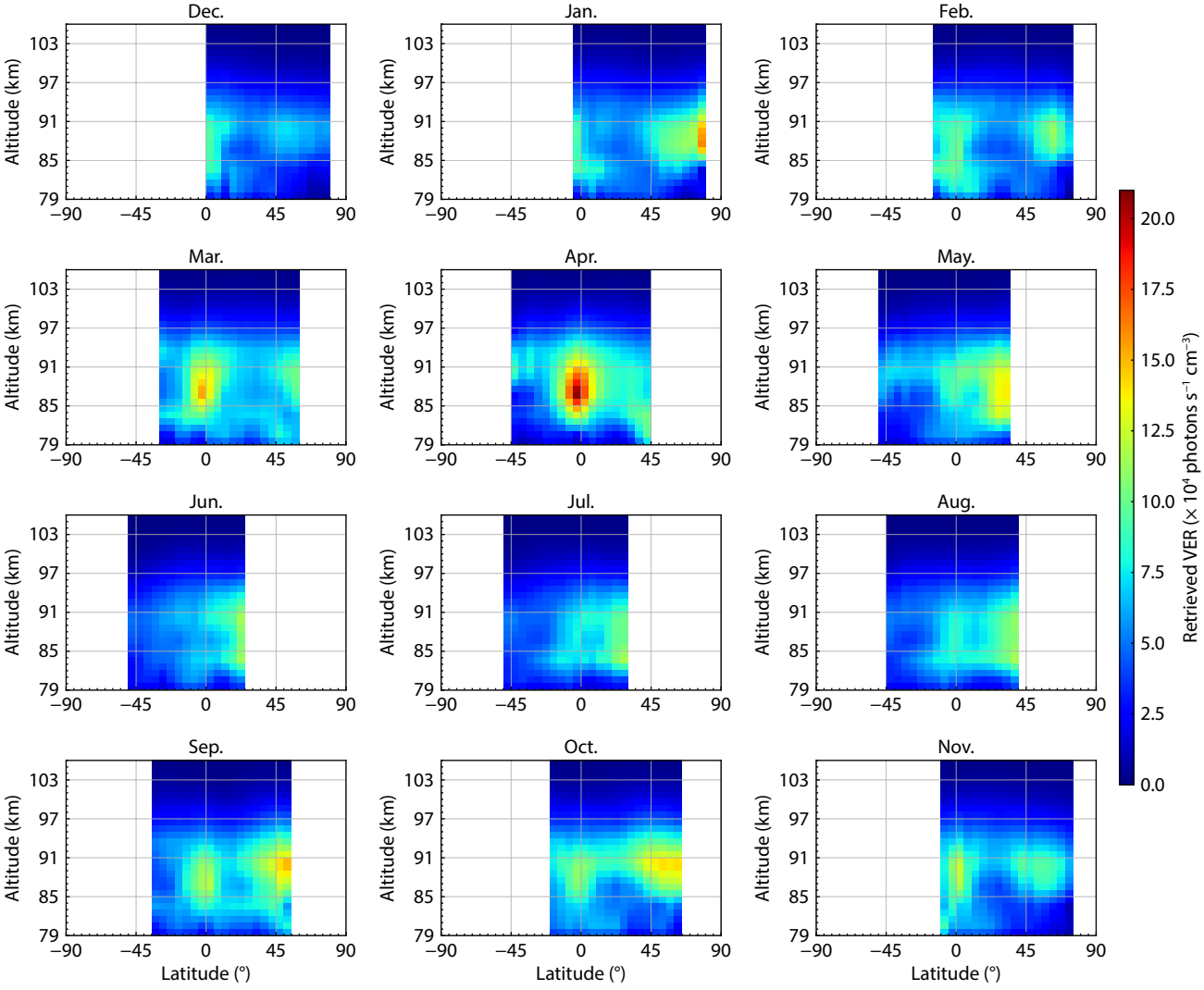

Figure 7. Spatial distribution of inverted VERs of $O_2$1.27 μm nightglow in 2007 after the interpolation.

nightglow VERs are consistent with those reported by Gao H et al. (2016). However, a comprehensive understanding of the underlying physical mechanisms requires further detailed investigation. Similar oscillation characteristics are observed in O_2A (0-1) band airglow, but the distribution of airglow intensity differs with latitude and altitude (López-González et al., 2004; Perminov and Pertsev, 2010). Perminov and Pertsev (2010) attributed the semi-annual variation in the O_2A (0-1) band to change in atomic oxygen density driven by atmospheric circulation. Besides, a study reported on global observations of the (O^1S) equatorial airglow by WINDII shows a strong local time control on the vertical distribution of VERs from the atomic oxygen green line airglow and concludes that it originates in tidal dynamics (Shepherd et al., 1995). Liu GP et al. (2008) indicated that vertical advection associated with the tides and the large-scale circulation plays a major role in airglow seasonal variations. The semi-annual variation, which is dominant around the equator, can be attributed mainly to the influence of diurnal tide (Gao H et al., 2016). The semi-annual variation in $O_2$1.27 μm nightglow might also be explored in conjunction with photochemical reaction components and atmospheric circulation transport processes.

As a key reactant in the production of $O_2$1.27 μm nightglow, atomic oxygen plays a crucial role in influencing photochemical reaction rates and, consequently, VERs intensity. The movement of atomic oxygen with atmospheric circulation impacts the intensity of $O_2$1.27 μm nightglow emissions. Ward (1999) simulated how tides affect atmospheric density, temperature, and atomic oxygen mixing ratio, which in turn regulate the behavior of nightglow emissions. He confirmed that nightglow emissions are enhanced with the increase of tidal amplitude, which was particularly obvious at low latitudes. Hays et al. (2003) highlighted the downward transport of atomic oxygen from the thermosphere by tides, enhancing nightglow emissions in the MLT region, while the weakened region of nightglow was associated with ascending tide motion. The modulating effect of the tides is strong on the atomic oxygen in the mesopause because of its long lifetime (Gao H et al., 2011). On the other hand, the collision of excited OH molecules with oxygen molecules or oxygen atoms can also produce O_2 nightglow, so there may be a certain correlation between O_2 nightglow and OH nightglow (Lednyts'kyy and von Savigny, 2020). Based on satellite observations, Marsh et al. (2006) indicated that the OH nightglow intensity and its temporal varia-

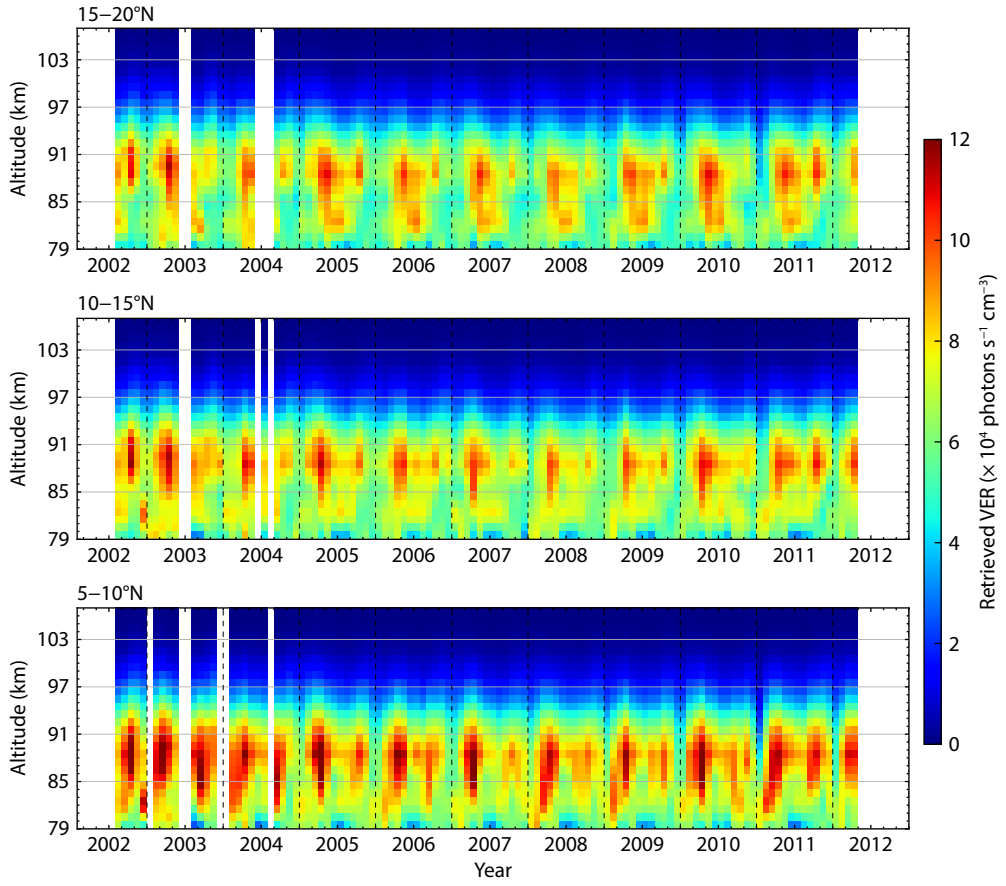

Figure 8. Inverted VERs of $O_2$1.27 μm nightglow in the time-altitude frame. From top to bottom, the latitudes are 5–10°N, 10–15°N, and 15–20°N, respectively. The white areas in the figure denote data gaps.

tion were strongly modulated by tides. Therefore, similar to the OH nightglow, the altitude-latitude distribution of O_2 nightglow emission is influenced by tides. Gao H et al. (2011) found that both the highest radiative intensity and the lowest peak height of $O_2$1.27 μm nightglow occurred over tropical areas during the spring and autumn equinoxes, with greater intensity observed during the spring equinox. Xu et al. report that the amplitude of diurnal tidal is larger during the March equinox than during the September equinox (Xu JY et al., 2009).

Our research (see Figure 9) confirms these equinoctial extremes, which we suggest may indeed be attributed to tidal influences. The downward transport of atomic oxygen increases under the influence of tides. The three-body reaction O + O + M→O_2* + M is the main source of the oxygen 1.27 μm emissions. These factors affect the intensity of O_2 nightglow emission during the spring equinox. Ward (1999) also pointed out that the modulation of airglow emission by tides is related to the phase and wavelength of tides. In addition, Zhu YJ (2016) identified a close relationship between the generation mechanism of oxygen airglow and solar ultraviolet radiation, affecting atomic oxygen concentration. The photochemical factors involved in airglow emissions, including formation reaction rates and quenching rates with the surrounding atmospheric components, are temperature-dependent (Liu WJ, 2016). Another study showed that the temperature at the mesopause region significantly responds to the electron precipitation during periods of intense solar activity (Zou ZC et al., 2020). Previous observations and model studies have proven that, when geomagnetic events are frequent, energetic particles stored in the magnetotail are accelerated Earthward to impact the dynamics and chemical composition of the middle and upper atmosphere (Sinnhuber et al., 2012; Yi W et al., 2018; Zou ZC et al., 2018). Solar activity's influence on MLT temperature (Zou ZC et al., 2020) and density (Yi W et al., 2018) can lead to changes in airglow emission intensity.

4. Conclusions

Based on limb spectra data from 2002 to 2012 collected by the SCIAMACHY payload, Volume Emission Rates (VERs) of $O_2$1.27 μm nightglow were obtained using a linear global optimization algorithm. The results are summarized as follows:

(1) A comparison between the $O_2$1.27 μm nightglow VERs data measured by the SABER payload and the linear inversion results of this study demonstrates consistency between the two datasets. The deviation between them is negligible, an average of -1.3×10^4 photons s^{-1} cm^{-3}, indicating that the linear inversion results accurately reflect the observed spatial and temporal distribution characteristics.

(2) The inverted VERs of $O_2$1.27 μm nightglow reveal a peak at 88 km above the equator in spring, particularly in April. Two other peaks occur between August and October, with the peak intensity

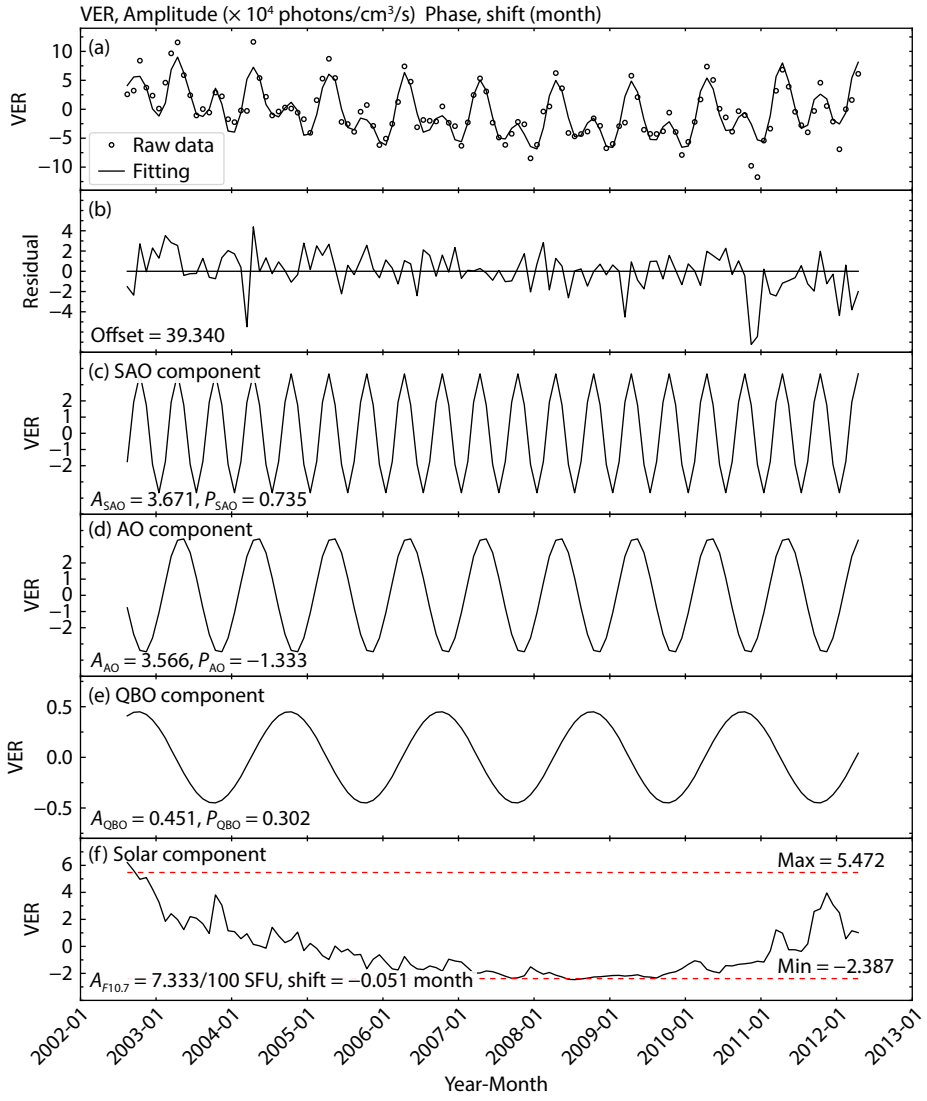

Figure 9. Harmonic analysis of $O_2$1.27 μm nightglow VERs at 10–15°N. In panel (a), the black dots represent the inverted data and the black line is the fitted curve. Panel (b) presents the offset and residual between the fitted values and the inverted data. Panels (c)–(f) present the fitting results of SAO, AO, QBO and solar components, respectively.

over the tropical region at 88 km weaker than the peak over 45°N at 90 km.

(3) The inverted VERs of $O_2$1.27 μm nightglow show a dependency on the 11-year solar cycle. That is, nightglow intensity strengthens with increasing solar activity and vice versa, displaying obvious semi-annual and annual variations.

Acknowledgments

This work was supported by the National Key R&D program of China (2021YFE0110200); the Project of Stable Support for Youth Team in Basic Research Field, CAS (YSBR-018); the National Natural Science Foundation of China (41831073, 42174196 and 42174212); the Chinese Meridian Project; the Specialized Research Fund for State Key Laboratories; and the International Partnership Program of Chinese Academy of Sciences. Grant No. 183311KYSB20200003.

References

Bertaux, J. L., Hauchecorne, A., Lefèvre, F., Bréon, F. M., Blanot, L., Jouglet, D., Lafrique, P., and Akaev, P. (2020). The use of the 1.27 μm O_2 absorption band for greenhouse gas monitoring from space and application to MicroCarb. *Atmos. Meas. Tech.*, *13*(6), 3329–3374. https://doi.org/10.5194/amt-13-3329-2020

Bovensmann, H., Burrows, J. P., Buchwitz, M., Frerick, J., Noël, S., Rozanov, V. V., Chance, K. V., and Goede, A. P. H. (1999). SCIAMACHY: mission objectives and measurement modes. *J. Atmos. Sci.*, *56*(2), 127–150. https://doi.org/10.1175/1520-0469(1999)056<0127:SMOAMM>2.0.CO;2

Gao, H., Xu, J. Y., Chen, G. M., Yuan, W., and Beletsky, A. B. (2011). Global distributions of OH and O_2 (1.27 μm) nightglow emissions observed by TIMED satellite. *Sci. China Technol. Sci.*, *54*(2), 447–456. https://doi.org/10.1007/s11431-010-4236-5

Gao, H., Xu, J. Y., and Chen, G. M. (2016). The responses of the nightglow emissions observed by the TIMED/SABER satellite to solar radiation. *J. Geophys. Res.: Space Phys.*, *121*(2), 1627–1642. https://doi.org/10.1002/2015JA021624

Hays, P. B., Kafkalidis, J. F., Skinner, W. R., and Roble, R. G. (2003). A global view of the molecular oxygen night airglow. *J. Geophys. Res.: Atmos.*, *108*(D20), 4646. https://doi.org/10.1029/2003JD003400

He, W. W., Wu, K. J., Wang, S. N., Fu, D., Wang, H. M., Liu, Q. X., and Yan, X. H. (2019). Observation technology of wind and temperature by onboard imaging interferometer with 1.27 μm air glow. *Opt. Optoelectronic Technol. (in Chinese)*, *17*(2), 72–78. https://doi.org/10.19519/j.cnki.1672-3392.2019.02.012

Howell, C. D., Michelangeli, D. V., Allen, M., Yuk L., Y., and Thomas, R. J. (1990). SME observations of $O_2(^1\Delta_g)$ nightglow: an assessment of the chemical production mechanisms. *Planet. Space Sci.*, *38*(4), 529–537. https://doi.org/10.1016/0032-0633(90)90145-G

Lednyts'kyy, O., and von Savigny, C. (2020). Photochemical modeling of molecular and atomic oxygen based on multiple nightglow emissions measured in situ during the Energy Transfer in the Oxygen Nightglow rocket campaign. *Atmos. Chem. Phys.*, *20*(4), 2221–2261. https://doi.org/10.5194/acp-20-2221-2020

Li, A. Q., Roth, C. Z., Pérot, K., Christensen, O. M., Bourassa, A., Degenstein, D. A., and Murtagh, D. P. (2020). Retrieval of daytime mesospheric ozone using OSIRIS observations of $O_2(a^1\Delta_g)$ emission. *Atmos. Meas. Tech.*, *13*(11), 6215–6236. https://doi.org/10.5194/amt-13-6215-2020

Li, A. Q., Roth, C. Z., Bourassa, A. E., Degenstein, D. A., Pérot, K., Christensen, O. M., and Murtagh, D. P. (2021). The OH (3-1) nightglow volume emission rate retrieved from OSIRIS measurements: 2001 to 2015. *Earth Syst. Sci. Data*, *13*(11), 5115–5126. https://doi.org/10.5194/essd-13-5115-2021

Li, H. C. (2023). Research on radiation correction method for ultraviolet limb atmospheric ozone detection [Ph. D. Thesis] (in Chinese). Changchun: Changchun Institute of Optics, Fine Mechanics and Physics, Chinese Academy of Sciences.

Liu, G. P., Shepherd, G. G., and Roble, R. G. (2008). Seasonal variations of the nighttime O(^{1}S) and OH airglow emission rates at mid-to-high latitudes in the context of the large-scale circulation. *J. Geophys. Res.: Space Phys.*, *113*(A6), A06302. https://doi.org/10.1029/2007JA012854

Liu, W. J. (2016). The detection and study on airglow spectra in middle and upper amosphere [Ph. D. Thesis] (in Chinese). Beijing: National Space Science Center, Chinese Academy of Sciences.

López-González, M. J., Rodríguez, E., Wiens, R. H., Shepherd, G. G., Sargoytchev, S., Brown, S., Shepherd, M. G., Aushev, V. M., López-Moreno, J. J., … Cho, Y. M. (2004). Seasonal variations of O_2 atmospheric and OH(6−2) airglowand temperature at mid-latitudes from SATI observations. *Ann. Geophys.*, *22*(3), 819–828. https://doi.org/10.5194/angeo-22-819-2004

Lopez-Moreno, J. J., Rodrigo, R., Moreno, F., Lopez-Puertas, M., and Molina, A. (1988). Rocket measurements of O_2 infrared atmospheric system in the nightglow. *Planet. Space Sci.*, *36*(5), 459–467. https://doi.org/10.1016/0032-0633(88)90105-5

Marsh, D. R., Smith, A. K., Mlynczak, M. G., and Russell III, J. M. (2006). SABER observations of the OH Meinel airglow variability near the mesopause. *J. Geophys. Res.: Space Phys.*, *111*(A10), A10S05. https://doi.org/10.1029/2005JA011451

McDade, I. C., Llewellyn, E. J., Greer, R. G. H., and Murtagh, D. P. (1987). ETON 6: a rocket measurement of the O_2 infrared atmospheric (0-0) band in the nightglow. *Planet. Space Sci.*, *35*(12), 1541–1552. https://doi.org/10.1016/0032-0633(87)90079-1

Perminov, V. I., and Pertsev, N. N. (2010). Seasonal and nighttime behaviors of emissions of hydroxyl and the atmospheric system of molecular oxygen of the midlatitude mesopause. *Geomagn. Aeron.*, *50*(4), 518–525. https://doi.org/10.1134/S0016793210040146

Rodgers, C. D. (2000). *Inverse Methods for Atmospheric Sounding: Theory and Practice*. Singapore: World Scientific.

Shepherd, G. G., McLandress, C., and Solheim, B. H. (1995). Tidal influence on O(^{1}S) Airglow emission rate distributions at the geographic equator as observed by WINDII. *Geophys. Res. Lett.*, *22*(3), 275–278. https://doi.org/10.1029/94GL03052

Sinnhuber, M., Nieder, H., and Wieters, N. (2012). Energetic particle precipitation and the chemistry of the mesosphere/lower thermosphere. *Surv. Geophys.*, *33*(6), 1281–1334. https://doi.org/10.1007/s10712-012-9201-3

Sun, K., Gordon, I. E., Sioris, C. E., Liu, X., Chance, K., and Wofsy, S. C. (2018). Reevaluating the use of O_2 $a^1\Delta_g$ spaceborne remote sensing of greenhouse gases. *Geophys. Res. Lett.*, *45*(11), 5779–5787. https://doi.org/10.1029/2018GL077823

Sun, K., Yousefi, M., Chan Miller, C., Chance, K., González Abad, G., Gordon, I. E., Liu, X., O'Sullivan, E., Sioris, C. E., and Wofsy, S. C. (2022). An optimal estimation-based retrieval of upper atmospheric oxygen airglow and temperature from SCIAMACHY limb observations. *Atmos. Meas. Tech.*, *15*(12), 3721–3745. https://doi.org/10.5194/amt-15-3721-2022

Tapping, K. F. (2013). The 10.7 cm solar radio flux ($F_{10.7}$). *Space Wea.*, *11*(7), 394–406. https://doi.org/10.1002/swe.20064

von Savigny, C. (2015). Variability of OH(3-1) emission altitude from 2003 to 2011: long-term stability and universality of the emission rate–altitude relationship. *J. Atmos. Solar-Terres. Phys.*, *127*, 120–128. https://doi.org/10.1016/j.jastp.2015.02.001

Wang, W. J., Luo, H. Y., Li, Z. W., Xiong, W., and Ma, J. J. (2021). Spatial and temporal distribution of O_2 a-band night airglow in mesosphere and lower thermosphere. *Acta Opt. Sin. (in Chinese)*, *41*(12), 1201001. https://doi.org/10.3788/AOS202141.1201001

Wang, Y. P., Li, X. Y., Chen, L. F., Zhang, Y., Zou, M. M., Zhang, H., and Zhu, S. Y. (2016). Overview of infrared limb sounding. *J. Remote Sens. (in Chinese)*, *20*(4), 513–527. https://doi.org/10.11834/jrs.20165302

Ward, W. E. (1999). A simple model of diurnal variations in the mesospheric oxygen nightglow. *Geophys. Res. Lett.*, *26*(23), 3565–3568. https://doi.org/10.1029/1999GL003661

Xu, J. Y., Smith, A. K., Liu, H. L., Yuan, W., Wu, Q., Jiang, G. Y., Mlynczak, M. G., Russell III, J. M., and Franke, S. J. (2009). Seasonal and quasi-biennial variations in the migrating diurnal tide observed by Thermosphere, Ionosphere, Mesosphere, Energetics and Dynamics (TIMED). *J. Geophys. Res.: Atmos.*, *114*(D13), D13107. https://doi.org/10.1029/2008JD011298

Xu, J. Y., Gao, H., Smith, A. K., and Zhu, Y. J. (2012). Using TIMED/SABER nightglow observations to investigate hydroxyl emission mechanisms in the mesopause region. *J. Geophys. Res.: Atmos.*, *117*(D2), D02301. https://doi.org/10.1029/2011JD016342

Yamamoto, H., Naito, I., Makino, T., and Sekiguchi, H. (1992). Altitude distribution of O_2 1.27μm nightglow emission observed by a rocket-borne radiometer. *J. Geomagn. Geoelectr.*, *44*(3), 207–221. https://doi.org/10.5636/jgg.44.207

Yang, X. J., Wang, H. M., and Wang, Y. M. (2020). Simulation and analysis on volume emission rate and limb radiation intensity of airglow at oxygen A(0, 0) band. *Chin. J. Space Sci. (in Chinese)*, *40*(6), 1039–1045. https://doi.org/10.11728/cjss2020.06.1039

Yi, W., Reid, I. M., Xue, X. H., Murphy, D. J., Hall, C. M., Tsutsumi, M., Ning, B. Q., Li, G. Z., Younger, J. P., … Dou, X. K. (2018). High- and middle-latitude neutral mesospheric density response to geomagnetic storms. *Geophys. Res. Lett.*, *45*(1), 436–444. https://doi.org/10.1002/2017GL076282

Zarboo, A., Bender, S., Burrows, J. P., Orphal, J., and Sinnhuber, M. (2018). Retrieval of $O_2(^1\Sigma)$ and $O_2(^1\Delta)$ volume emission rates in the mesosphere and lower thermosphere using SCIAMACHY MLT limb scans. *Atmos. Meas. Tech.*, *11*(1), 473–487. https://doi.org/10.5194/amt-11-473-2018

Zhu, Y. J. (2016). Atomic oxygen derived from SCIAMACHY O(^{1}S) and OH airglow measurements in the mesopause region [Ph. D. Thesis]. Fakultät für Mathematik und Naturwissenschaften, Bergischen Universität Wuppertal.

Zou, Z. C., Xue, X. H., Shen, C. L., Yi, W., Wu, J. F., Chen, T. D., and Dou, X. K. (2018). Response of mesospheric HO_2 and O_3 to large solar proton events. *J. Geophys. Res.: Space Phys.*, *123*(7), 5738–5746. https://doi.org/10.1029/2018JA025481

Zou, Z. C., Xue, X. H., Yi, W., Shen, C. L., Yang, C. Y., Tang, Y. H., Chen, T. D., and Dou, X. K. (2020). Response of the high-latitude upper mesosphere to energetic electron precipitation. *Astrophys. J.*, *893*(1), 55. https://doi.org/10.3847/1538-4357/ab7eb0